

Probing Inelastic Dark Matter at the LHC, FASER and STCF

Chih-Ting Lu,^{1,2,*} Jianfeng Tu,^{1,†} and Lei Wu^{1,‡}

¹*Department of Physics and Institute of Theoretical Physics,
Nanjing Normal University, Nanjing, 210023, China*

²*CAS Key Laboratory of Theoretical Physics, Institute of Theoretical Physics,
Chinese Academy of Sciences, Beijing 100190, P. R. China*

(Dated: September 4, 2023)

Abstract

In this work, we explore the potential of probing the inelastic dark matter (DM) model with an extra $U(1)_D$ gauge symmetry at the Large Hadron Collider, ForwArd Search ExpeRiment and Super Tau Charm Factory. To saturate the observed DM relic density, the mass splitting between two light dark states has to be small enough, and thus leads to some distinctive signatures at these colliders. By searching for the long-lived particle, the displaced muon-jets, the soft leptons, and the mono-photon events, we find that the inelastic DM mass in the range of 1 MeV to 210 GeV could be tested.

* ctlu@njnu.edu.cn

† tujf@nnu.edu.cn

‡ leiwu@njnu.edu.cn

CONTENTS

I. Introduction	2
II. Inelastic dark matter model	4
III. Signatures of inelastic DM at colliders	6
A. LLPs at the FASER	8
B. Displaced Muon-Jet at the LHC	9
C. Soft Lepton Pair at the LHC	10
D. Mono-photon Event at the STCF	13
E. Numerical Results and Discussions	14
IV. Conclusion	18
Acknowledgments	18
References	18

I. INTRODUCTION

Despite the strong astrophysical and cosmological evidence to support the existence of dark matter (DM) [1, 2], its nature still remains a mystery. It is widely believed that Standard Model (SM) particles may interact with DM through forces other than gravity [3]. The Weakly Interacting Massive Particle (WIMP) is one of the most popular dark matter candidates [4, 5]. However, null results of searching for WIMPs have imposed stringent constraints on its properties in the mass range of GeV to TeV [6, 7]. For instance, the spin-independent (SI) DM-nucleon scattering cross section is limited to 6.5×10^{-48} cm² at the DM mass of 30 GeV [8, 9]. This motivates the recent studies of the light DM models that can avoid the conventional constraints. To explore the sub-GeV DM, various new proposals and experiments have been proposed [10, 11].

However, in the thermal freeze-out scenario, the sub-GeV DM models usually suffer from various astrophysical and cosmological constraints. For example, the s-wave annihilation of light DM is not favored by the cosmic microwave background (CMB), which requires

the DM mass should be heavier than about 10 GeV [12]. Additionally, the DM particles with the mass less than 1 MeV is tightly constrained by the Big Bang Nucleosynthesis (BBN) [13]. Nevertheless, there exist some exceptions that can evade these bounds, such as the DM models with the p-wave annihilation [14], the inelastic DM models [15], the asymmetric DM models [16], and the freeze-in mechanism DM models [17]. Among them, the inelastic DM models that were motivated by the explanation of the DAMA excess [15] have recently gained considerable attention [18–42]. If only the lighter DM state is present in the current Universe, the up-scattering in DM-nucleon interactions becomes insensitive to direct detection¹, and the primary elastic DM-nucleon scattering occurs at the one-loop level [19]. Consequently, these models can evade the limits from direct detection [43].

In this paper, we investigate the prospect of probing the inelastic DM model with an additional $U(1)_D$ gauge symmetry at colliders. The mass splitting of two dark states is induced by the interaction between the dark Higgs field and the DM sector, and the transition between two dark states is mediated by the new $U(1)_D$ gauge boson. The collider signatures of inelastic DM at accelerators strongly depend on two key parameters: the ground state DM mass (M_{χ_1}) and the mass splitting between the excited and ground DM states ($\Delta_\chi \equiv M_{\chi_2} - M_{\chi_1}$). These two parameters are also associated with the lifetime of the excited DM state. For $M_{\chi_1} \lesssim 5$ GeV and $\Delta_\chi < 0.5M_{\chi_1}$, the fixed target experiments [44–46] and low energy e^+e^- colliders such as BaBar [47], Belle II [48], BESIII [49] and Super Tau Charm Factory (STCF) [50] offer powerful avenues for searching for inelastic DM. On the other hand, for $M_{\chi_1} \lesssim 15$ GeV and $\Delta_\chi \lesssim 0.1M_{\chi_1}$, LLP experiments like ForwArd Search ExpeRiment (FASER) [51, 52], MAssive Timing Hodoscope for Ultra-Stable neutral-pArticles (MATHUSLA) [53], SeaQuest [54], the COnpact Detector for EXotics at LHCb (CODEX-b) [55] and A Laboratory for Long-Lived eXotics (AL3X) [56] can explore the remaining parameter space. In the intermediate DM mass range of $2 \text{ GeV} \lesssim M_{\chi_1} \lesssim 200$ GeV with $\Delta_\chi \lesssim 0.2M_{\chi_1}$, the Large Hadron Collider (LHC) remains the primary machine for probing inelastic DM.

The structure of this paper is expanding as follows. In Sec. II, we recapitulate the inelastic DM model with an $U(1)_D$ gauge symmetry. In Sec. III, we then study the signatures of inelastic DM at the FASER, LHC, and STCF. Finally, we summarize our findings in Sec. IV.

¹ Note people can consider cosmic ray-boosted inelastic DM for the up-scattering in DM-nucleon interactions as shown in Ref. [33, 34]

II. INELASTIC DARK MATTER MODEL

In this section, we briefly review the inelastic DM models with an $U(1)_D$ gauge symmetry and focus on the fermionic DM candidates². In addition to the SM particles, a singlet complex scalar field Φ as well as a Dirac fermion field χ are involved. We assign the $U(1)_D$ charges for Φ and χ as $Q(\Phi) = +2$ and $Q(\chi) = +1$, respectively. All SM particles are neutral under the $U(1)_D$ symmetry and cannot be directly coupled to the dark sector. The relevant gauge invariant and renormalizable Lagrangian for this model can be written as

$$\begin{aligned}\mathcal{L} = & \mathcal{L}_{SM} - \frac{1}{4}X_{\mu\nu}X^{\mu\nu} - \frac{1}{2}\sin\epsilon X_{\mu\nu}B^{\mu\nu} + \mathcal{D}^\mu\Phi^\dagger\mathcal{D}_\mu\Phi \\ & - \mu_\Phi^2\Phi^\dagger\Phi + \lambda_\Phi(\Phi^\dagger\Phi)^2 - \lambda_{\mathcal{H}\Phi}\mathcal{H}^\dagger\mathcal{H}\Phi^\dagger\Phi \\ & - \bar{\chi}(i\mathcal{D}^\mu - M_\chi)\chi - \left(\frac{\xi}{2}\Phi^\dagger\bar{\chi}^c\chi + H.c.\right),\end{aligned}\quad (1)$$

where $X_{\mu\nu}$ and $B_{\mu\nu}$ are field strength tensors of $U(1)_D$ and $U(1)_Y$ gauge fields, respectively. ϵ is the kinematic mixing angle between $X_{\mu\nu}$ and $B_{\mu\nu}$, μ_Φ is the parameter with the same dimension as mass, and λ_Φ , $\lambda_{\mathcal{H}\Phi}$ are dimensionless parameters and ξ is assumed to be a positive, real and dimensionless parameter. \mathcal{H} is the SM-like scalar doublet field and we expand \mathcal{H} and Φ in the unitary gauge to the following form,

$$\mathcal{H} = \frac{1}{\sqrt{2}} \begin{pmatrix} 0 \\ v + h \end{pmatrix}, \quad \Phi = \frac{1}{\sqrt{2}}(v_X + h_X), \quad (2)$$

where v and v_X are vacuum expectation values of \mathcal{H} and Φ , respectively. The $U(1)_D$ is broken spontaneously by $\langle\Phi\rangle = v_X/\sqrt{2}$, and electroweak symmetry is broken spontaneously as usual by $\langle\mathcal{H}\rangle = (0, v/\sqrt{2})$.

We then diagonalize the $U(1)$ gauge kinetic term in Eq. (1) by redefining the gauge fields via the following transformation [22, 37, 57] :

$$\begin{pmatrix} B^\mu \\ X^\mu \end{pmatrix} = \begin{pmatrix} 1 & \eta \\ 0 & \eta/\epsilon \end{pmatrix} \begin{pmatrix} B_p^\mu \\ X_p^\mu \end{pmatrix}. \quad (3)$$

The covariant derivative is given by $\mathcal{D}_\mu = \partial_\mu + i(g_D Q_X + g_1 \eta Q_Y)X_\mu + ig_1 Q_Y B_\mu + ig_2 T^3 W_\mu^3$, where W_μ^3 , B_μ , and X_μ correspond to the gauge potentials associated with the gauge groups

² The scalar inelastic DM models can be found in Ref. [18, 19, 25, 30, 36, 38]. Since we will study the on-shell Z' productions and Z' mainly decays to DM states, the predictions in our analysis can be applied to scalar inelastic DM models as well.

$SU(2)_L$, $U(1)_Y$, and $U(1)_X$, respectively. The gauge couplings are denoted as g_2 , g_1 , and g_D . The gauge fields before mixing are represented by B_p^μ and X_p^μ . Additionally, we define $\eta \equiv \epsilon/\sqrt{1-\epsilon^2}$, and Q_X represents the $U(1)_D$ charge of either Φ or χ .

After performing a $GL(2, R)$ rotation to diagonalize the kinetic terms, followed by an $O(3)$ rotation to diagonalize the 3×3 neutral gauge boson mass matrix, the mass eigenstates can be expressed through the corresponding transformation as [37] :

$$\begin{pmatrix} B_p^\mu \\ W^3 \\ X_p^\mu \end{pmatrix} = \begin{pmatrix} c_W & -s_W c_X & s_W s_X \\ s_W & c_W c_X & -c_W s_X \\ 0 & s_X & c_X \end{pmatrix} \begin{pmatrix} A \\ Z \\ Z' \end{pmatrix}, \quad (4)$$

where the s_W and c_W are the sine and cosine values of the weinberg angle, and the new gauge mixing angle can be written as

$$\theta_X = \frac{1}{2} \arctan\left(\frac{-2s_W\eta}{1-s_W^2\eta^2-\Delta_Z}\right), \quad (5)$$

where $\Delta_Z = M_X^2/M_{Z_0}^2$, $M_X^2 = g_D^2 Q_X^2 v_X^2$ and $M_{Z_0}^2 = (g_1^2 + g_2^2)v^2/4$, which M_X and M_Z are the masses of two $U(1)$ gauge bosons before mixing. Finally, the photon becomes massless, and two heavier gauge boson mass eigenvalues are

$$M_{Z,Z'} = \frac{M_{Z_0}^2}{2} [(1 + s_W^2\eta^2 + \Delta_Z) \pm \sqrt{(1 - s_W^2\eta^2 + \Delta_Z)^2 + 4s_W^2\eta^2}], \quad (6)$$

which valid for $\Delta_Z < 1 - s_W^2\eta^2$. Considering the assumption $\epsilon \ll 1$, we find $M_{Z'} \approx M_X$ from Eq. (6) and the interactions of Z' and SM fermions for the linear order approximation in ϵ can be written as

$$\mathcal{L}_{Z' \bar{f}f} = -\epsilon e c_W Q_f \bar{f} \gamma^\mu f Z'_\mu, \quad (7)$$

where Q_f is the electric charge of SM fermions.

The Dirac fermion field can be further decomposed into two Majorana fermion fields χ_1 , χ_2 as

$$\begin{aligned} \chi &= \frac{1}{\sqrt{2}}(\chi_2 + i\chi_1), \\ \chi_2 &= \chi_2^c, \quad \chi_1 = \chi_1^c. \end{aligned} \quad (8)$$

After the breaking of $U(1)_D$ gauge symmetry, the DM parts of Eq. (1) can be expanded as

$$\begin{aligned} \mathcal{L}_\chi = & \frac{1}{2} \sum_{n=1,2} \bar{\chi}_n (i\cancel{d} - M_\chi) \chi_n - i \frac{g_D}{2} (\bar{\chi}_2 \chi_1 - \bar{\chi}_1 \chi_2) \cancel{X} \\ & - \frac{\xi}{2} (v_X + h_X) (\bar{\chi}_2 \chi_2 - \bar{\chi}_1 \chi_1). \end{aligned} \quad (9)$$

We summarize some interesting features from the above equation. First, there is a residual Z_2 symmetry via Krauss-Wilczek mechanism [58] which the $U(1)_D$ gauge symmetry is broken into its Z_2 subgroup [18]. Only $\chi_{1,2}$ are Z_2 -odd and can be DM candidate(s). Second, the mass splitting between χ_1 and χ_2 is triggered from the $\Phi^\dagger \bar{\chi}^c \chi$ interaction after the symmetry breaking and can be written as

$$\Delta_\chi = 2\xi v_X. \quad (10)$$

We then assign $M_{\chi_2} > M_{\chi_1}$ with the form,

$$M_{\chi_{1,2}} = M_\chi \mp \xi v_X. \quad (11)$$

Before closing this section, we have to mention that the scalar sector in this model is not the focus of this work. More details for the scalar sector in fermionic inelastic DM models and relevant search strategies can be found in Ref. [28, 30, 36]. We can properly choose model parameters to satisfy all constraints from the scalar sector part in this study.

III. SIGNATURES OF INELASTIC DM AT COLLIDERS

We will discuss the production of inelastic DM at the LHC and classify the signal signatures depending on the decay length of χ_2 . First of all, the UFO model file of the inelastic DM model is generated by `FeynRules` [59] and then we apply `MadGraph5_aMC@NLO` [60] to generate Monte Carlo events and calculate cross sections for the following signal process,

$$pp \rightarrow A' \rightarrow \chi_2 \chi_1. \quad (12)$$

We consider a centre-of-mass energy of $\sqrt{s} = 14$ TeV and fix the following model parameters,

$$M_{Z'} = 3M_{\chi_1}, \quad \alpha_D = \frac{g_D^2}{4\pi} = 0.1, \quad \epsilon = 0.01, \quad (13)$$

but vary M_{χ_1} and Δ_χ in the range below,

$$M_{\chi_1}/\text{GeV} = [5, 100], \quad \Delta_\chi/\text{GeV} = [0.01, 0.1], \quad (14)$$

with the step length 5 GeV and 0.01 GeV for M_{χ_1} and Δ_χ , respectively.

The time of flight for χ_2 is automatically calculated in the Madgraph5@NLO. In the approximation $M_{Z'} \gg M_{\chi_2} \sim M_{\chi_1} \gg M_l$, the partial decay rate for $\chi_2 \rightarrow \chi_1 l^+ l^-$ can be written as [19]

$$\Gamma(\chi_2 \rightarrow \chi_1 l^+ l^-) \simeq \frac{4\epsilon^2 \alpha_{\text{em}} \alpha_D \Delta_\chi^5}{15\pi M_{Z'}^4} \quad (15)$$

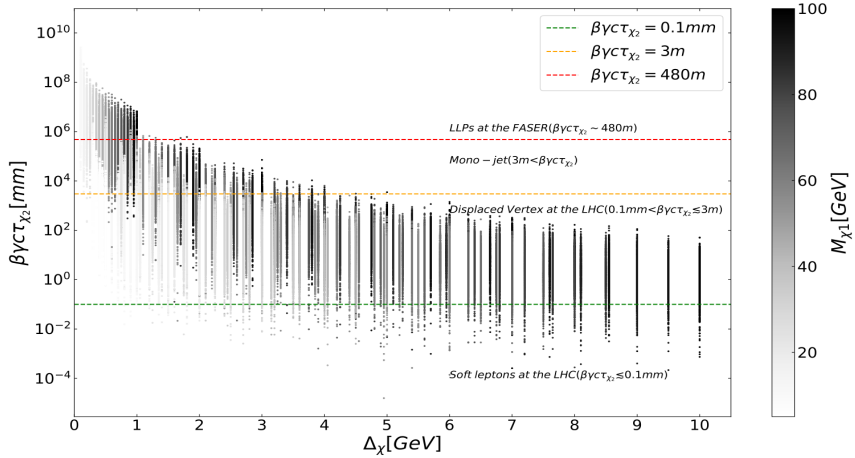


FIG. 1. The relationship of $(\Delta_\chi, \beta\gamma c\tau_{\chi_2})$ with varying M_{χ_1} . The three dashed lines represent different special lab frame decay length numbers, $\beta\gamma c\tau_{\chi_2} = 0.1$ mm (green), $\beta\gamma c\tau_{\chi_2} = 3$ m (orange), and $\beta\gamma c\tau_{\chi_2} = 480$ m (red).

where $l = e, \mu$ and $\alpha_{\text{em}} \simeq 1/137$ is the fine structure constant. It's clear to see that once we reduce the values of ϵ , Δ_χ , and M_{χ_1} , the lifetime of χ_2 will enhance. In the Fig. 1, we display the relations of M_{χ_1} and ϵ to the χ_2 decay length. We can find the behaviors in numerical results are consistent with the approximated formula in Eq. (15).

In addition, we use three dashed lines in Fig. 1 to illustrate our search strategies for inelastic DM at collider experiments. Specifically, if the lab frame decay length of χ_2 is as long as $\beta\gamma c\tau_{\chi_2} \simeq \mathcal{O}(500)$ m, the FASER is an ideal detector to search for inelastic DM as shown in the red dashed line in Fig. 1. Here, γ is the Lorentz factor, β is the velocity of χ_2 , and $\tau_{\chi_2} = 1/\Gamma_{\chi_2}$ is the proper decay time of χ_2 . The details for this analysis can be found in Sec. III A. If χ_2 generates the displaced vertex at the LHC with 0.1 mm $< \beta\gamma c\tau_{\chi_2} \lesssim 3$ m, the displaced muon-jet (DMJ) signature is sensitive to search for inelastic DM in this parameter space as shown in the regions below the orange dashed line in Fig. 1. We study this possibility in Sec. III B. Furthermore, if χ_2 is prompt decay ($\beta\gamma c\tau_{\chi_2} \lesssim 0.1$ mm), the soft leptons searches at the LHC can be applied to this situation as shown in the regions below the green dashed line in Fig. 1. We recast the ATLAS analysis [61] for soft leptons signatures in Sec. III C. Finally, if χ_2 is the LLP with $\beta\gamma c\tau_{\chi_2} > 3$ m, the mono-jet searches can indirectly impose constraints on this model as shown in the regions above the orange

dashed line in Fig. 1. However, the mono-jet constraints from the LHC are much weaker than the above ones, so we will not show the recasting for these constraints in this work. Finally, as a complementary study to cover the searches of sub-GeV inelastic DM, we utilize the mono-photon signature to search for inelastic DM at STCF. More details for this analysis will be presented in Sec. III D.

A. LLPs at the FASER

As we know, the B-factories can explore LLPs, but the restriction of their center-of-mass energies forces the upper bound of the mass of LLPs to be less than about 10 GeV [62]. On the other hand, the ATLAS/CMS detectors at the LHC are not sensitive to the new particles with mass less than $\mathcal{O}(10)$ GeV. Therefore, a new lifetime frontier detector to search for $\mathcal{O}(10)$ GeV BSM LLPs is needed.

In this subsection, we introduce a new detector called FASER, which has been built around the LHC to study LLPs that interact with SM particles weakly and have light masses [63]. These particles have attracted significant attention as they could potentially explain DM and reconcile discrepancies between theoretical predictions and low-energy experiments [64–67]. Traditional detectors at the LHC primarily focus on heavier new particles in the central regions and lack the necessary sensitivity to detect light, weakly-coupled particles that are produced in the forward direction. Additionally, these particles, known as LLPs, can be highly boosted in the forward direction, traveling a macroscopic distance before decaying. Therefore, a detector located along the beamline axis in the forward region could enable the detection of light LLPs. The FASER experiment aims to address this by constructing a detector which is 480 meters downstream from the ATLAS interaction point (IP). Furthermore, there is a proposal for FASER 2, which would be constructed from 2024-2026 to collect data during the HL-LHC era from 2026 to 2035 [52]. In the current investigation, we assume that LLPs produced near the IP travel along the beam axis and decay into SM particles, which can be detected by FASER. Therefore, LLPs within the acceptance angle of FASER should have high energies in the TeV range, as the decay products from LLPs would also possess energies close to the TeV scale. The full process is described as follows:

$$pp \rightarrow \chi_2 + \chi_1, \chi_2 \text{ travels } \sim 480\text{m, then } \chi_2 \rightarrow \chi_1 f\bar{f}. \quad (16)$$

The FASER detector is located in a region surrounded by rock, and the forward LHC infrastructure, including magnets and absorbers, helps to suppress potential background processes. Detailed simulations using FLUKA technology [68, 69] have confirmed low radiation levels in LHC tunnels, with the radiative process associated with muons being the dominant background. To further mitigate backgrounds, a scintillating charged particle veto layer is employed in front of the detector [22]. Specifically, the FASER detector rejects high-energy charged particles, primarily muons, and protons to minimize additional troublesome backgrounds. With these technical measures, the background levels are considered negligible.

To enhance the trigger efficiency at low energies, FASER requires a significant deposition of visible energy from the decay products of χ_2 , with $E_{\text{vis}} > 100$ GeV. The specific parameters for the two-phase detectors, FASER and FASER 2, are cylindrical in shape, characterized by their length (L) and radius (R):

$$\begin{aligned} \textbf{FASER} : L &= 1.5\text{m}, \quad R = 0.1\text{m}, \\ \textbf{FASER 2} : L &= 5\text{m}, \quad R = 1\text{m}. \end{aligned} \tag{17}$$

Additionally, the integrated luminosity, \mathcal{L} , for FASER and FASER 2 is 150 fb^{-1} and 3 ab^{-1} , respectively.

B. Displaced Muon-Jet at the LHC

In this subsection, we focus on the signature of DMJ [70–76] from inelastic DM models at the LHC. In the scenario where $M_{Z'} > M_{\chi_1} + M_{\chi_2}$, the Z' can be on-shell produced in association with a QCD jet at the LHC [77]. Subsequently, the Z' decays into χ_1 and χ_2 , and within the tracker system of the ATLAS and CMS detectors, the χ_2 particle further decays into χ_1 and two muons. However, due to the high boost of χ_2 , the resulting pair of muons from its decay becomes highly collimated, making it challenging to pass the muon isolation criteria. This phenomenon gives rise to a novel object known as a muon-jet. Our particular interest lies in a displaced dimuon vertex associated with a jet and missing momentum. This process is referred to as the DMJ signature, which is considered a particularly clean signal.

The search strategy for this kind of signature was proposed by Ref. [19, 22]. Our analysis of the DMJ signature follows the methodology outlined in the above two references. In their

work, most of the relevant backgrounds were found to be relatively negligible. It is worth noting that displaced vertex tracks can also be present in QCD-initiated processes, which may involve the production and subsequent decay of LLPs such as B or K hadrons into π and μ . The authors of Ref. [19] assume that the probability of such events is small but provide an approximate upper bound on the probability of a QCD-initiated event producing a hard leading jet with transverse momentum $p_T^j > 120$ GeV and two displaced muons with transverse momenta $p_T^\mu > 5$ GeV, considering the small mass splitting between χ_2 and χ_1 . Additionally, in order to ensure the displacement of the muon tracks, a minimum transverse impact parameter $d_\mu > 1$ mm is imposed. Furthermore, it is known that if the decay length of χ_2 is sufficiently long to allow the production of two muons will through completely the tracking system, allowing for more precise track reconstruction. Hence, a requirement is imposed that the radial displacement ($R_{\chi_2}^{xy}$) of the χ_2 decay vertex is less than 30 cm. In summary, the selection criteria for the signal region of DMJ signature encompass the following conditions:

$$\begin{aligned}
 \mathbf{DMJ} : & p_T^j > 120 \text{ GeV}, \\
 & p_T^\mu > 5 \text{ GeV}, \\
 & d_\mu > 1 \text{ mm}, \\
 & R_{\chi_2}^{xy} < 30 \text{ cm}.
 \end{aligned} \tag{18}$$

The selection criteria outlined above have been carefully chosen in anticipation of an integrated luminosity of $\mathcal{L} = 3 \text{ ab}^{-1}$ at the High-Luminosity LHC. It is worth noting that extensive studies conducted by the authors of Ref. [19] have demonstrated that these criteria effectively reduce the backgrounds to a negligible level.

C. Soft Lepton Pair at the LHC

In this subsection, we investigate the search for inelastic DM models through the soft lepton pair(SLP) analysis. In our concerned process, the final state particles consist of two leptons are originated from χ_2 decay via the off-shell Z' boson. We utilize the data collected by the ATLAS detector, corresponding to an integrated luminosity of 139 fb^{-1} at $\sqrt{s} = 13$ TeV, as described in Ref. [61], events with missing transverse momentum and two same-flavor, oppositely charged, low transverse momentum leptons are selected. To ensure

consistency with the ATLAS analysis, we employ the analysis file provided by the CheckMATE2 program package [78]. The CheckMATE2 program allows us to determine whether the processes involved in inelastic DM models are excluded or not at a 95% Confidence Level (C.L.), by comparing them with the results reported in Ref. [61]. In our simulations, event samples are generated using `MadGraph5_aMC@NLO`(version 2.7.2). We didn't put any pre-selections in parton level event generation, but the ME-PS matching was performed using the CKKW-L merging [79] scheme with the merging scale set to 15 GeV. To enforce an initial state radiation(ISR) topology, at least one parton in the final state was required to have a transverse momentum greater than 50 GeV. After the event reconstruction, all events entering the signal regions (SRs) undergo a common set of event selections, which is summarized in Table I.

Variable	Event selection
Number of leptons	= 2 leptons
Leading lepton p_T [GeV]	$p_T^{\ell_1} > 5$
$\Delta R_{\ell\ell}$	$\Delta R_{ee} > 0.3, \Delta R_{\mu\mu} > 0.05$
Lepton charge and flavor	$e^\pm e^\mp, \mu^\pm \mu^\mp$
J/ψ invariant mass veto [GeV]	veto $3.0 < m_{\ell\ell} < 3.2$
Lepton invariant mass [GeV]	$3 < m_{ee} < 60, 1 < m_{\mu\mu} < 60$
E_T^{miss} [GeV]	≥ 120
$m_{\tau\tau}$ [GeV]	$m_{\tau\tau} < 0$ or $m_{\tau\tau} > 160$
Number of jets	≥ 1
Number of b -tagged jets	= 0
Leading jet p_T [GeV]	≥ 100
$\min(\Delta\phi(\text{jets}, \mathbf{p}_T^{\text{miss}}))$	> 0.4
$\Delta\phi(j_1, \mathbf{p}_T^{\text{miss}})$	≥ 2.0

TABLE I. The event selection requirements applied to all events entering SRs for soft lepton pair analysis.

According to Table I, the event selections for our signal events require exactly two leptons of the same flavor with opposite charges. We order the leading lepton (ℓ_1) and subleading

lepton (ℓ_2) by the size of their transverse momentum. The $p_T^{\ell_1}$ is required to be larger than 5 GeV, which helps to reduce backgrounds from fake/nonprompt (FNP) leptons. And the subleading lepton' p_T ($p_T^{\ell_2}$) will have different constraints on different SRs. The lepton pair is also required to have a separation $\Delta R_{\ell\ell}$, with $\Delta R_{\mu\mu}$ larger than 0.05 for a muon pair and ΔR_{ee} larger than 0.3 for an electron pair. This requirement improves the efficiency of event reconstruction by avoiding overlapping electron showers in the electromagnetic calorimeter. The final state leptons must have opposite charge and same flavor. Furthermore, the invariant mass of the lepton pair ($m_{\ell\ell}$) should fall outside the range [3.0, 3.2] GeV, which removes contributions from the J/ψ decays. The $m_{\ell\ell}$ is also required to be less than 60 GeV to reduce contributions from on-shell Z boson decays. Requirements on the minimum angular separation between the lepton candidates ($\Delta R_{\ell\ell}$) and $m_{\ell\ell}$ remove events in which an energetic photon produces collinear lepton pairs. The variable $m_{\tau\tau}$ represents the invariant mass approximation of a pair of τ leptons undergoing leptonically decaying processes. It is defined as $m_{\tau\tau} = \text{sign}(m_{\tau\tau}^2) \sqrt{|m_{\tau\tau}^2|}$, which is the signed square root of $m_{\tau\tau}^2 \equiv 2p_{\ell_1}p_{\ell_2}(1 + \zeta_1)(1 + \zeta_2)$, where p_{ℓ_1}, p_{ℓ_2} are four-momentum of two leptons, while ζ_1, ζ_2 are the parameters in solving $\mathbf{p}_T^{\text{miss}} = \zeta_1 \mathbf{p}_T^{\ell_1} + \zeta_2 \mathbf{p}_T^{\ell_2}$. In certain events, the $m_{\tau\tau}$ variable can be less than zero. This occurs when one of the lepton momenta has a smaller magnitude compared to the transverse missing energy (E_T^{miss}) and points in the hemisphere opposite to the momentum imbalance vector ($\mathbf{p}_T^{\text{miss}}$). In order to mitigate backgrounds originating from the Z boson decays into $\tau^+\tau^-$, events falling within the range of $0 < m_{\tau\tau} < 160$ GeV are excluded. This selection criterion achieves an efficiency exceeding 80 percent for the analyzed signals.

Additionally, for the events in our research process, almost invisible momentum is carried by χ_1 , these requirements on E_T^{miss} suggest that the process our concerned is recoiling against additional hadronic activities, like ISR. All events are therefore required to have at least one jet with $p_T^j > 100$ GeV, therefore, the missing transverse energy (E_T^{miss}) is required to be greater than 120 GeV in this analysis, even higher in some SRs. Additional jets in the event are also required to be separated from the $\mathbf{p}_T^{\text{miss}}$ by $\min(\Delta\phi(\text{jets}, \mathbf{p}_T^{\text{miss}})) > 0.4$ in order to suppress the impact of jet energy mismeasurement on E_T^{miss} . Our research process, focusing on the final state particles with two leptons, events with one or more b -tagged jets are vetoed to reduce backgrounds from SM $t\bar{t}$ production.

D. Mono-photon Event at the STCF

In this subsection, we discuss the search for the light Z' decay to $\chi_1\chi_2$ via the mono-photon signature at the future STCF which is an e^+e^- collider project with a peak luminosity of $10^{35} \text{ cm}^{-2}\text{s}^{-1}$ and operating in $\sqrt{s} = 2$ to 7 GeV [80, 81]. The process of interest is $e^+e^- \rightarrow \gamma Z' \rightarrow \gamma(\chi_1\chi_2)$. However, this process is subject to both reducible and irreducible backgrounds due to the limited detection capability. The main reducible SM backgrounds include the processes $e^+e^- \rightarrow \gamma f\bar{f}$ and $e^+e^- \rightarrow \gamma\gamma(\gamma)$, where the final state particles are emitted in the solid angle region not covered by the detectors. The process $e^+e^- \rightarrow \gamma e^+e^-$, where the final state electron and positron are collinear with the beam directions, receives a significant contribution from t -channel diagrams. The irreducible SM backgrounds to our process are the processes $e^+e^- \rightarrow \gamma\nu_\ell\bar{\nu}_\ell$, where $\nu_\ell = \nu_e, \nu_\mu, \nu_\tau$ are SM neutrinos.

In this study, we apply specific cuts on the final state photon to reduce background events. These cuts are based on the analysis from BESIII [82] and are used for both reducible and irreducible SM backgrounds. Specifically, we impose the conditions $E_\gamma > 25 \text{ MeV}$ in the barrel region ($|z_\gamma| < 0.8$) and $E_\gamma > 50 \text{ MeV}$ in the end-caps region ($0.92 > |z_\gamma| > 0.86$), where E_γ is the photon energy and $z_\gamma \equiv \cos\theta_\gamma$ with θ_γ being the relative angle between the electron beam axis and the photon momentum. However, applying these cuts alone does not effectively suppress the contribution from reducible backgrounds, which remains significant. To further address this, we introduce an additional cut based on momentum conservation in the transverse direction and energy conservation [83–85]. As an example, considering the reducible background process $e^+e^- \rightarrow \gamma e^+e^-$, we use energy conservation in the center-of-mass frame and transverse momentum conservation to obtain the following relations:

$$E_\gamma + E_1 + E_2 = \sqrt{s}, \quad (19)$$

$$E_\gamma \sin\theta_\gamma - E_1 \sin\theta_1 - E_2 \sin\theta_2 = 0. \quad (20)$$

Here, E_γ , E_1 , and E_2 are energies of the final state photon, electron, and positron, respectively, and θ_γ , θ_1 , and θ_2 represent their respective polar angles. By imposing the condition that both $|\cos\theta_{1,2}|$ are greater than or equal to $|\cos\theta_b|$, where $|\cos\theta_b|$ is the polar angle at the boundary of the sub-detector where the final state electron and positron are emitted.

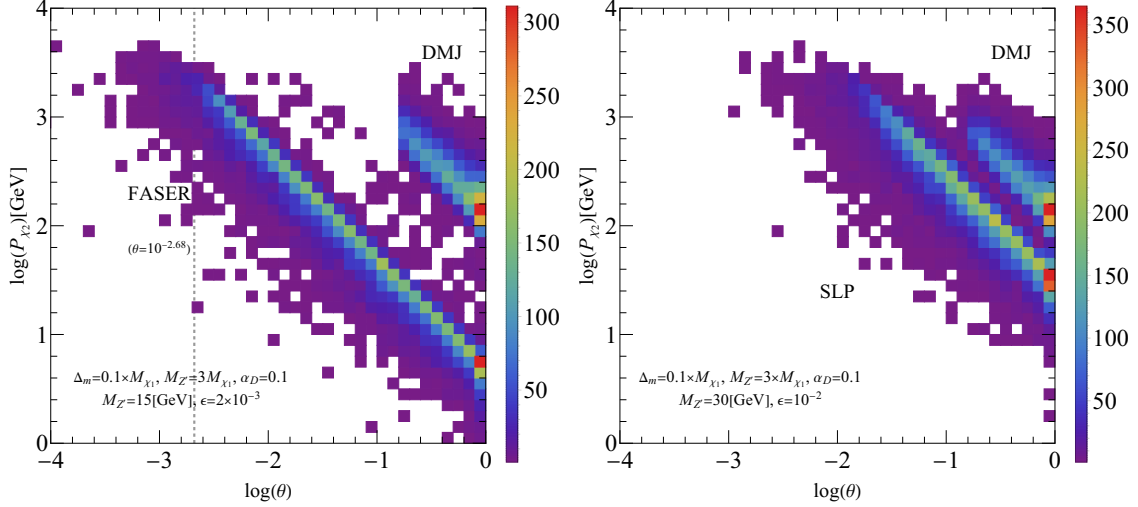


FIG. 2. The $P_{\chi_2} - \theta$ distribution of χ_2 . The left panel is under the search strategies of FASER and LHC(DMJ) with $M_{\chi_2} = 5.5$ GeV and $M_{Z'} = 15$ GeV. The right panel is under the search strategies of DMJ and SLP at the LHC with $M_{\chi_2} = 11$ GeV and $M_{Z'} = 30$ GeV. The vertical line (dashed grey) in the left panel indicates the decay length in the lab frame for FASER 2 (480 m), which tells us there exist sensitive regions with χ_2 when $\theta < 10^{-2.68}$.

We request $|\cos \theta_b| \geq 0.95$, and the final photon energy cut,

$$E_\gamma > E_b(\theta_\gamma) = \frac{\sqrt{s}}{(1 + \frac{\sin \theta_\gamma}{\sin \theta_b})}. \quad (21)$$

The energy cut E_b is determined by the polar angle θ_b and ensures that the final state photon lies outside the boundary region. In this work, we aim to probe the light Z' decay to $\chi_1 \chi_2$ via the mono-photon signature at $\sqrt{s} = 4, 7$ GeV, and corresponding to $\mathcal{L} = 30 \text{ ab}^{-1}$.

E. Numerical Results and Discussions

In Fig 2, we present the event distribution over the magnitude of the spatial momentum P of χ_2 and its angle θ along the beam line under different search strategies on various benchmark points. In the left panel, the $P_{\chi_2} - \theta$ distribution in the lower left area corresponds to the LLPs search at the FASER, while the distribution in the upper right corner represents the DMJ search at the LHC. These distributions are obtained for fixed $M_{Z'} = 15$ GeV and $\epsilon = 2 \times 10^{-3}$. The dashed grey line denotes the acceptance angle for FASER 2 ($\theta < 10^{-2.68}$), illustrating that the FASER detector has sensitivity primarily to highly boosted particles

with a very small angle relative to the beam line. The reason for this is that the χ_2 produced in this process has a very low transverse momentum (P_T), which is nearly equal to M_{χ_2} , and it is emitted in the forward direction, with its trajectories collimated along the beam-line. The DMJ event distribution tells us the high off-beam-line sensitivity because there exists a high P_T jet (> 120 GeV) back to Z' . Since we only require $P_T^\mu > 5$ GeV in this analysis, it leads to the lower threshold of $P_T^{\chi_2} \geq 50$ GeV ($P_T^\mu \sim \Delta \times P_T^{\chi_2}$). We can clearly find that the distribution pattern in the left panel indicates a kinematic overlap between these two strategies. Next, the right panel in Fig. 2 corresponds to the SLP searches at 13 TeV LHC and the DMJ searches at the LHC. These distributions are obtained for fixed $M_{Z'} = 30$ GeV and $\epsilon = 10^{-2}$. The lower left $P_{\chi_2} - \theta$ distribution represents the SLP search, while the upper right part corresponds to the DMJ search. We observe a larger kinematic overlap between these two strategies compared to the left panel, which is consistent with the results presented in Fig. 4.

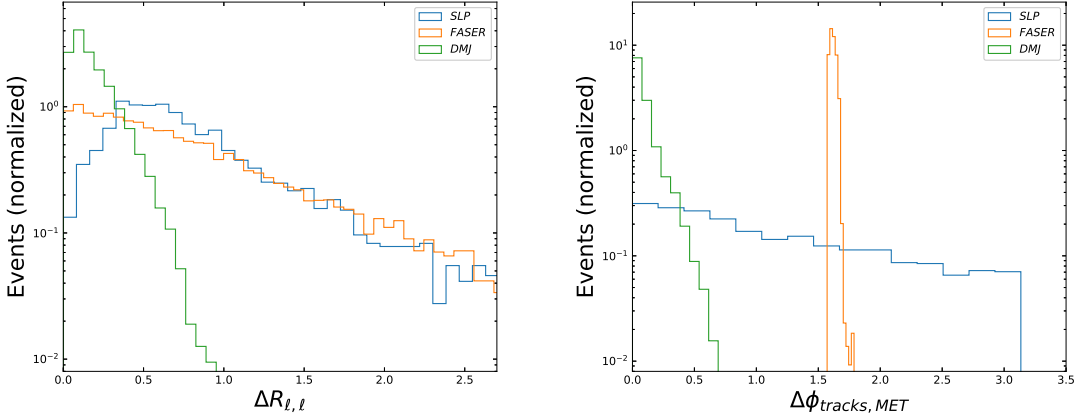


FIG. 3. The left panel represents the ΔR distributions between two leptons in the final state from the χ_2 decays, and the right panel shows the $\Delta\phi$ distributions between the spatial momentum of the lepton tracks and the missing energy.

In Fig 3, we provide the kinematic distributions of $\Delta R_{\ell\ell}$ and $\Delta\phi_{\text{Tracks, MET}}$, with the fixed parameter points in their own probing regions, $M_{\chi_1} = 1$ GeV and $\epsilon = 10^{-2}$ for the FASER, $M_{\chi_1} = 10$ GeV and $\epsilon = 10^{-2}$ for the LHC (DMJ), and $M_{\chi_1} = 160$ GeV and $\epsilon = 7 \times 10^{-2}$ for the LHC (SLP) respectively, to illustrate their distinct kinematic properties in these three search strategies. In the left panel of Fig 3, we present the opening angle distribution of

two leptons, $\Delta R_{\ell\ell}$, originating from the decay of χ_2 . The STCF signature is not considered in this analysis as its mass range is predominantly below the GeV scale. The DMJ search at LHC exhibits the largest collinear feature of a lepton pair compared to the other two search strategies because of the initial high P_T jet in this signature. In contrast, the SLP searches at the LHC show a relatively weak collimation among the three strategies. The right panel of Fig 3 displays the relative azimuthal angle between the lepton tracks and the missing energy, $\Delta\phi_{\text{Tracks, MET}}$. We observe that the DMJ signature at the LHC exhibits a smaller $\Delta\phi_{\text{Tracks, MET}}$ compared to the signature at the FASER. This difference arises from the fact that the DMJ process involves an initial high p_T jet causing a high energy Z' recoiling this jet, therefore, leading the production of Z' to be relatively collinear. In contrast, the situation at the FASER results in larger relative angles between the produced χ_1 and χ_2 . For the SLP searches, which involve matching and merging effects of QCD jets, the distribution of $\phi_{\text{Tracks, MET}}$ tends to be more evenly distributed. Therefore, $\Delta R_{\ell\ell}$ and $\Delta\phi_{\text{Tracks, MET}}$ distributions provide insights into the kinematic characteristics of different search strategies.

In our analyses, we take the benchmark parameters as [19, 21, 22, 30, 38]: $M_{Z'} = 3M_{\chi_1}$, $\alpha_D \equiv g_D^2/4\pi = 0.1$, and $\Delta_\chi = 0.1M_{\chi_1}$. After applying the above event selections and search strategies, we present the final results regarding the projected sensitivity for different search strategies. These results will be displayed in the (M_{χ_1}, ϵ) plane for $10^{-3} \text{ GeV} < M_{\chi_1} < 10^3 \text{ GeV}$. This region is particularly interesting as it contains extensive areas that are still unconstrained by current experimental measurements. The strategies proposed in this study aim to cover a large portion of these unconstrained regions related to this model.

Our main findings are illustrated in Fig. 4, which includes both light gray regions and colored contour regions. The light gray regions represent the current experimental constraints derived from experiments such as BaBar [89], LEP [87, 88], and CMS 13 TeV DMJ [77]. Besides, the boundary lines derived from fixed target experiments E137 and LSND can be found in Ref. [21]. In contrast, the colored contour regions depict the projected sensitivities obtained through the four strategies employed in our analysis³. Finally, the black bold line represents the parameter space where the abundance of χ_1 agrees with the measured DM

³ The FASER results from our analyses are slightly different from the corresponding results in Ref. [22].

The main reasons for these differences stem from the absence of consideration for the production of DM states from meson decays, the distinction in c_W resulting from the Z' coupling to fermions in the SM, and the selection of different size parameters by the detectors.

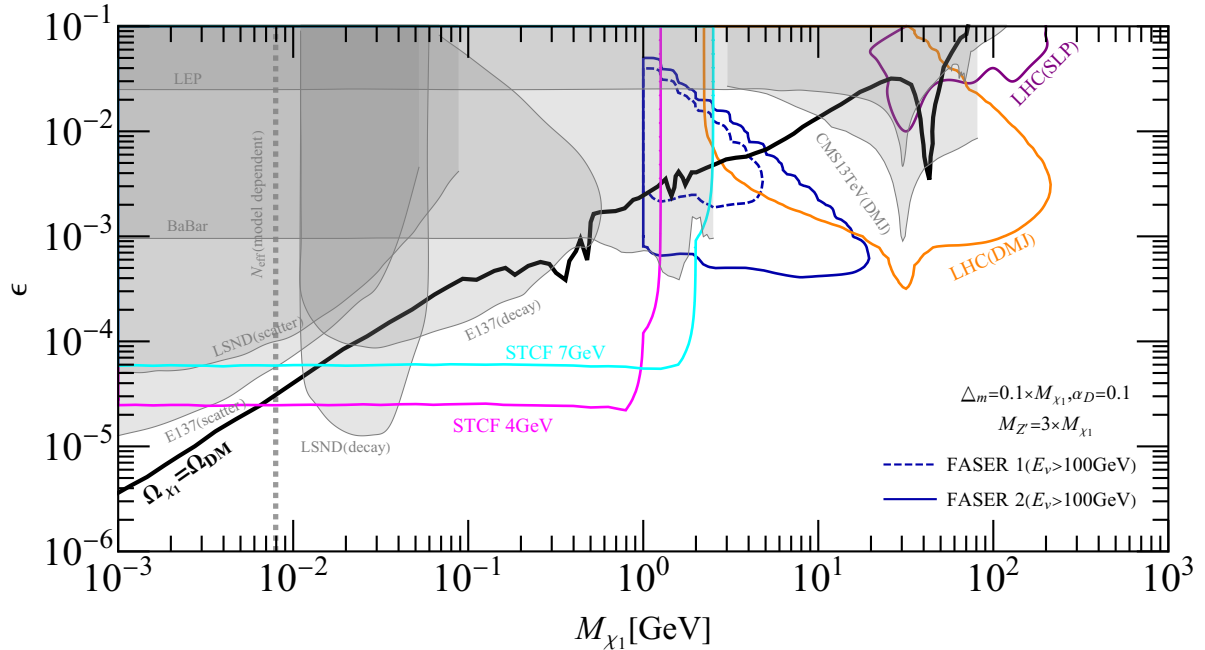


FIG. 4. The existing bounds (gray) and sensitivities (color) for the fermionic inelastic DM models in the (M_{χ_1}, ϵ) plane with fixed $\alpha_D=0.1$, $M_{Z'} = 3M_{\chi_1}$, $\Delta_{\chi}=0.1M_{\chi_1}$. The black contour represents the region where the abundance of χ_1 matches the observed DM relic density [19, 27, 86]. The light gray regions represent the excluded regions from LEP [87, 88] and BaBar [89] as well as LSND and SLAC E137 beam-dumps [21]. The colored contours indicate the projected reach of different strategies. Specifically, the orange contours correspond to the reach of searches at ATLAS and CMS [22, 90], while the dark dashed blue and dark blue contours represent the reach of FASER1 and FASER2 [51, 52, 65]. The purple region shows the excluded region from the soft lepton pair search at ATLAS based on recast experimental analyses [61]. The sensitivity of the STCF search via monophoton is displayed in magenta and cyan for $\sqrt{s} = 4, 7$ GeV [50].

relic density [19, 27, 86]. As illustrated in Fig 4, our analysis demonstrates that all the search strategies employed in this work are capable of probing the parameter space that is not excluded by current constraints.

In this study, we have chosen a fixed ratio of the Z' mass to the χ_1 mass, specifically $M_{Z'}/M_{\chi_1} = 3$. However, if the value of $M_{Z'}/M_{\chi_1}$ is increased, both the relic density curve and projected sensitivities line in our search strategies would shift upward compared to that in Fig. 4. Inversely, the relic density curve and projected sensitivities line shift downward when $M_{Z'}/M_{\chi_1}$ decreases. On the other hand, we have set the mass splitting $\Delta_{\chi}/M_{\chi_1} = 0.1$

in our analysis. If Δ_χ/M_{χ_1} is decreased, the relic density curve would shift downward, but the projected results of different strategies will shift upward to disappear sensitivity while the Δ_χ/M_{χ_1} is small enough so we need the other search strategies to further explore these parameter space. It is important to note that while our work demonstrates good complementary among the four strategies in probing inelastic DM, there are still other exploration methods that can be pursued including time-delayed tracks at the LHC [22, 91] and other LLPs experiments like MATHUSLA [53], CODEX-b [55], AL3X [56], and so on.

IV. CONCLUSION

In this work, we study the prospects of searching for the inelastic DM at colliders. Due to the constraint of DM relic density, the mass splitting between the heavier and lighter dark states should be small to achieve the coannihilation, which leads to some unconventional signatures in this model. For the inelastic DM mass in the range of 1 MeV to 210 GeV, we find that most of the parameter space that can provide the correct relic density could be probed by searching for the long-lived particles at the FASER, the displaced muon-jets and soft leptons at the LHC, and the mono-photon events at the STCF.

ACKNOWLEDGMENTS

We thank Wei Liu, Yu Zhang and Bin Zhu for the helpful discussions. The work is supported by the National Natural Science Foundation of China (NNSFC) under grant No. 12147228 and Project 12047503 supported by NSFC.

[1] V. Trimble, *Ann. Rev. Astron. Astrophys.* **25**, 425 (1987).

[2] L. Barack et al., *Class. Quant. Grav.* **36**, 143001 (2019), 1806.05195.

[3] M. Pospelov, A. Ritz, and M. B. Voloshin, *Phys. Lett. B* **662**, 53 (2008), 0711.4866.

[4] J. L. Feng, *Ann. Rev. Astron. Astrophys.* **48**, 495 (2010), 1003.0904.

[5] M. Bauer and T. Plehn, *Yet Another Introduction to Dark Matter: The Particle Physics Approach*, vol. 959 of *Lecture Notes in Physics* (Springer, 2019), 1705.01987.

[6] M. Schumann, *J. Phys. G* **46**, 103003 (2019), 1903.03026.

- [7] F. Kahlhoefer, Int. J. Mod. Phys. A **32**, 1730006 (2017), 1702.02430.
- [8] J. Aalbers et al. (LZ) (2022), 2207.03764.
- [9] E. Aprile et al. (XENON) (2023), 2303.14729.
- [10] S. Knapen, T. Lin, and K. M. Zurek, Phys. Rev. D **96**, 115021 (2017), 1709.07882.
- [11] T. Lin, SciPost Phys. Lect. Notes **43**, 1 (2022).
- [12] T. Lin, H.-B. Yu, and K. M. Zurek, Phys. Rev. D **85**, 063503 (2012), 1111.0293.
- [13] K. M. Nollett and G. Steigman, Phys. Rev. D **91**, 083505 (2015), 1411.6005.
- [14] S. Matsumoto, Y.-L. S. Tsai, and P.-Y. Tseng, JHEP **07**, 050 (2019), 1811.03292.
- [15] D. Tucker-Smith and N. Weiner, Phys. Rev. D **64**, 043502 (2001), hep-ph/0101138.
- [16] K. M. Zurek, Phys. Rept. **537**, 91 (2014), 1308.0338.
- [17] C. Dvorkin, T. Lin, and K. Schutz, Phys. Rev. Lett. **127**, 111301 (2021), 2011.08186.
- [18] S. Baek, P. Ko, and W.-I. Park, Phys. Lett. B **747**, 255 (2015), 1407.6588.
- [19] E. Izaguirre, G. Krnjaic, and B. Shuve, Phys. Rev. D **93**, 063523 (2016), 1508.03050.
- [20] F. D'Eramo, K. Hambleton, S. Profumo, and T. Stefaniak, Phys. Rev. D **93**, 103011 (2016), 1603.04859.
- [21] E. Izaguirre, Y. Kahn, G. Krnjaic, and M. Moschella, Phys. Rev. D **96**, 055007 (2017), 1703.06881.
- [22] A. Berlin and F. Kling, Phys. Rev. D **99**, 015021 (2019), 1810.01879.
- [23] G. Mohlabeng, Phys. Rev. D **99**, 115001 (2019), 1902.05075.
- [24] Y.-D. Tsai, P. deNiverville, and M. X. Liu, Phys. Rev. Lett. **126**, 181801 (2021), 1908.07525.
- [25] N. Okada and O. Seto, Phys. Rev. D **101**, 023522 (2020), 1908.09277.
- [26] P. Ko, T. Matsui, and Y.-L. Tang, JHEP **10**, 082 (2020), 1910.04311.
- [27] M. Duerr, T. Ferber, C. Hearty, F. Kahlhoefer, K. Schmidt-Hoberg, and P. Tunney, JHEP **02**, 039 (2020), 1911.03176.
- [28] M. Duerr, T. Ferber, C. Garcia-Cely, C. Hearty, and K. Schmidt-Hoberg, JHEP **04**, 146 (2021), 2012.08595.
- [29] Y. Ema, F. Sala, and R. Sato, Eur. Phys. J. C **81**, 129 (2021), 2007.09105.
- [30] D. W. Kang, P. Ko, and C.-T. Lu, JHEP **04**, 269 (2021), 2101.02503.
- [31] N. F. Bell, J. B. Dent, B. Dutta, S. Ghosh, J. Kumar, and J. L. Newstead, Phys. Rev. D **104**, 076013 (2021), 2103.05890.
- [32] B. Batell, J. Berger, L. Darmé, and C. Frugueule (2021), 2106.04584.

[33] N. F. Bell, J. B. Dent, B. Dutta, S. Ghosh, J. Kumar, J. L. Newstead, and I. M. Shoemaker, Phys. Rev. D **104**, 076020 (2021), 2108.00583.

[34] J.-C. Feng, X.-W. Kang, C.-T. Lu, Y.-L. S. Tsai, and F.-S. Zhang, JHEP **04**, 080 (2022), 2110.08863.

[35] J. Guo, Y. He, J. Liu, and X.-P. Wang, JHEP **04**, 024 (2022), 2111.01164.

[36] J. Li, T. Nomura, and T. Shimomura, JHEP **09**, 140 (2022), 2112.12432.

[37] A. Filimonova, S. Junius, L. Lopez Honorez, and S. Westhoff, JHEP **06**, 048 (2022), 2201.08409.

[38] E. Bertuzzo, A. Scaffidi, and M. Taoso, JHEP **08**, 100 (2022), 2201.12253.

[39] Y. Gu, L. Wu, and B. Zhu, Phys. Rev. D **106**, 075004 (2022), 2203.06664.

[40] J. Li, L. Su, L. Wu, and B. Zhu, JCAP **04**, 020 (2023), 2210.15474.

[41] M. Mongillo, A. Abdullahi, B. B. Oberhauser, P. Crivelli, M. Hostert, D. Massaro, L. M. Bueno, and S. Pascoli, Eur. Phys. J. C **83**, 391 (2023), 2302.05414.

[42] S. Heeba, T. Lin, and K. Schutz (2023), 2304.06072.

[43] M. Carrillo González and N. Toro, JHEP **04**, 060 (2022), 2108.13422.

[44] H. Merkel et al. (A1), Phys. Rev. Lett. **106**, 251802 (2011), 1101.4091.

[45] S. Abrahamyan, Z. Ahmed, K. Allada, D. Anez, T. Averett, A. Barbieri, K. Bartlett, J. Beacham, J. Bono, J. R. Boyce, et al., Phys. Rev. Lett. **107**, 191804 (2011), URL <https://link.aps.org/doi/10.1103/PhysRevLett.107.191804>.

[46] H. Merkel, P. Achenbach, C. Ayerbe Gayoso, T. Beranek, J. Beričić, J. C. Bernauer, R. Böhm, D. Bosnar, L. Correa, L. Debenjak, et al. (A1 Collaboration), Phys. Rev. Lett. **112**, 221802 (2014), URL <https://link.aps.org/doi/10.1103/PhysRevLett.112.221802>.

[47] A. Filippi (BABAR), EPJ Web Conf. **218**, 06001 (2019).

[48] I. Adachi et al. (Belle-II) (2022), 2212.03066.

[49] M. Ablikim et al. (BESIII), Phys. Lett. B **839**, 137785 (2023), 2209.13893.

[50] D. A. Epifanov (SCTF), Phys. Atom. Nucl. **83**, 944 (2020).

[51] A. Ariga et al. (FASER) (2018), 1812.09139.

[52] A. Ariga et al. (FASER) (2019), 1901.04468.

[53] C. Alpigiani et al. (MATHUSLA), in *Snowmass 2021* (2022), 2203.08126.

[54] M. X. Liu and P. E. Reimer (SeaQuest) (2023).

[55] G. Aielli et al. (2022), 2203.07316.

[56] D. Dercks, H. K. Dreiner, M. Hirsch, and Z. S. Wang, Phys. Rev. D **99**, 055020 (2019), 1811.01995.

[57] J. D. Wells, pp. 283–298 (2008), 0803.1243.

[58] L. M. Krauss and F. Wilczek, Phys. Rev. Lett. **62**, 1221 (1989), URL <https://link.aps.org/doi/10.1103/PhysRevLett.62.1221>.

[59] N. D. Christensen and C. Duhr, Comput. Phys. Commun. **180**, 1614 (2009), 0806.4194.

[60] J. Alwall, R. Frederix, S. Frixione, V. Hirschi, F. Maltoni, O. Mattelaer, H. S. Shao, T. Stelzer, P. Torrielli, and M. Zaro, JHEP **07**, 079 (2014), 1405.0301.

[61] G. Aad et al. (ATLAS), Phys. Rev. D **101**, 052005 (2020), 1911.12606.

[62] M. Acevedo, A. Blackburn, N. Blinov, B. Shuve, and M. Stone, JHEP **09**, 154 (2021), 2105.12744.

[63] M. Battaglieri et al., in *U.S. Cosmic Visions: New Ideas in Dark Matter* (2017), 1707.04591.

[64] A. J. Krasznahorkay, M. Csatlós, L. Csige, Z. Gácsi, J. Gulyás, M. Hunyadi, I. Kuti, B. M. Nyakó, L. Stuhl, J. Timár, et al., Phys. Rev. Lett. **116**, 042501 (2016), URL <https://link.aps.org/doi/10.1103/PhysRevLett.116.042501>.

[65] J. L. Feng, I. Galon, F. Kling, and S. Trojanowski, Phys. Rev. D **97**, 035001 (2018), 1708.09389.

[66] G. W. Bennett, B. Bousquet, H. N. Brown, G. Bunce, R. M. Carey, P. Cushman, G. T. Danby, P. T. Debevec, M. Deile, H. Deng, et al. (Muon g-2 Collaboration), Phys. Rev. D **73**, 072003 (2006), URL <https://link.aps.org/doi/10.1103/PhysRevD.73.072003>.

[67] C. Böhm and P. Fayet, Nuclear Physics B **683**, 219 (2004), ISSN 0550-3213, URL <https://www.sciencedirect.com/science/article/pii/S0550321304000306>.

[68] A. Ferrari, P. R. Sala, A. Fasso, and J. Ranft (2005).

[69] T. Böhlen, F. Cerutti, M. Chin, A. Fassò, A. Ferrari, P. Ortega, A. Mairani, P. Sala, G. Smirnov, and V. Vlachoudis, Nuclear Data Sheets **120**, 211 (2014), ISSN 0090-3752, URL <https://www.sciencedirect.com/science/article/pii/S0090375214005018>.

[70] M. Baumgart, C. Cheung, J. T. Ruderman, L.-T. Wang, and I. Yavin, JHEP **04**, 014 (2009), 0901.0283.

[71] C. Cheung, J. T. Ruderman, L.-T. Wang, and I. Yavin, JHEP **04**, 116 (2010), 0909.0290.

[72] A. Falkowski, J. T. Ruderman, T. Volansky, and J. Zupan, JHEP **05**, 077 (2010), 1002.2952.

[73] E. Izaguirre and B. Shuve, Phys. Rev. D **91**, 093010 (2015), 1504.02470.

[74] M. Kim, H.-S. Lee, M. Park, and M. Zhang, Phys. Rev. D **98**, 055027 (2018), 1612.02850.

[75] S. Dube, D. Gadkari, and A. M. Thalapillil, Phys. Rev. D **96**, 055031 (2017), 1707.00008.

[76] M. Zhang, Phys. Rev. D **104**, 055008 (2021), 2104.06988.

[77] A. Hayrapetyan et al. (CMS) (2023), 2305.11649.

[78] D. Dercks, N. Desai, J. S. Kim, K. Rolbiecki, J. Tattersall, and T. Weber, Comput. Phys. Commun. **221**, 383 (2017), 1611.09856.

[79] L. Lonnblad and S. Prestel, JHEP **03**, 019 (2012), 1109.4829.

[80] A. Y. Barniakov (Super Charm-Tau Factory), PoS **LeptonPhoton2019**, 062 (2019).

[81] J. Liang, Z. Liu, and L. Yang, JHEP **05**, 184 (2022), 2111.15533.

[82] M. Ablikim, M. N. Achasov, S. Ahmed, M. Albrecht, A. Amoroso, F. F. An, Q. An, J. Z. Bai, O. Bakina, R. Baldini Ferroli, et al. (BESIII Collaboration), Phys. Rev. D **96**, 112008 (2017), URL <https://link.aps.org/doi/10.1103/PhysRevD.96.112008>.

[83] Y. Zhang, W.-T. Zhang, M. Song, X.-A. Pan, Z.-M. Niu, and G. Li, Phys. Rev. D **100**, 115016 (2019), URL <https://link.aps.org/doi/10.1103/PhysRevD.100.115016>.

[84] Z. Liu, Y.-H. Xu, and Y. Zhang, JHEP **06**, 009 (2019), 1903.12114.

[85] Y. Zhang, W.-T. Zhang, M. Song, X.-A. Pan, Z.-M. Niu, and G. Li, Phys. Rev. D **100**, 115016 (2019), 1907.07046.

[86] E. Izaguirre, Y. Kahn, G. Krnjaic, and M. Moschella, Phys. Rev. D **96**, 055007 (2017), URL <https://link.aps.org/doi/10.1103/PhysRevD.96.055007>.

[87] A. Hook, E. Izaguirre, and J. G. Wacker, Adv. High Energy Phys. **2011**, 859762 (2011), 1006.0973.

[88] D. Curtin, R. Essig, S. Gori, and J. Shelton, JHEP **02**, 157 (2015), 1412.0018.

[89] J. P. Lees et al. (BaBar), Phys. Rev. Lett. **119**, 131804 (2017), 1702.03327.

[90] E. Izaguirre, G. Krnjaic, and B. Shuve, Phys. Rev. D **93**, 063523 (2016), URL <https://link.aps.org/doi/10.1103/PhysRevD.93.063523>.

[91] J. Liu, Z. Liu, and L.-T. Wang, Phys. Rev. Lett. **122**, 131801 (2019), 1805.05957.